

On plasma parameters of a self-organized plasma jet at atmospheric pressure

J. Schäfer^a, F. Sigeneger, R. Foest, D. Loffhagen, and K.-D. Weltmann

INP Greifswald, Felix-Hausdorff-Str. 2, 17489 Greifswald, Germany

Received 14 May 2010

Published online 14 September 2010 – © EDP Sciences, Società Italiana di Fisica, Springer-Verlag 2010

Abstract. Electron temperature and electron concentration in the active zone of a miniaturized radio frequency (RF) non-thermal atmospheric pressure plasma jet in argon have been determined using two independent approaches: the spectroscopic measurement of the broadening of Balmer H_β and H_γ lines and a time-dependent, spatially two-dimensional fluid model of a single discharge filament. The plasma source has been configured as a capacitively coupled RF jet (27.12 MHz, 8 W generator output power) with two outer ring electrodes around a quartz capillary with diameter of 4.0 mm between which Ar flows at typical rates of 0.3 slm. The discharge has been operated in a self-organized mode, where equidistant, stationary filaments rotate regularly with a constant frequency at the inner wall of the outer capillary. For the purpose of calculating the spectral line broadening different models applicable at higher electron concentration have been evaluated. Resulting electron concentrations are between 2.2 and $3.3 \times 10^{14} \text{ cm}^{-3}$. The calculation according to the line broadening model provides electron temperatures between 20 000 and 30 000 K which is in agreement with the results of the fluid model calculations. Here, a broad radial profile with a maximal value of about 22 000 K in the centre of the column and an electron concentration of about $7 \times 10^{13} \text{ cm}^{-3}$ have been obtained. Moreover, the results of the model calculations reveal a structural change of the filament from the dielectric surface through the sheath to the column. The axially inhomogeneous region has an extension of about 0.5 mm. In the column a concentration of about 10^{13} cm^{-3} has been found for the excited argon atoms, whose collisions with electrons represent the most important ionization channel there.

1 Introduction

Miniaturized non-thermal jet plasmas represent an emerging technique for local surface treatment at ambient atmosphere. Applications include surface cleaning, etching, surface activation, film deposition, and the reduction of micro-organisms. Numerous different discharge geometries and excitation principles have been proposed [1–8]. An overview is given e.g. in references [9,10]. Moreover, several technical solutions are available on the market.

The particular plasma source under study here is a capacitively coupled capillary jet (27.12 MHz) with two outer ring electrodes around a quartz capillary between which a gas (Ar) flows at rates of about 0.3 slm. The plasma can be divided into different spatial regions: the active discharge zone in the capillary, i.e., the region with the electric field between the electrodes, the effluent region, i.e., the plasma plume, and the remote region. During thin film deposition, thin film producing agents are added in small quantities downstream the active discharge region, where the effluent develops. It could be shown in previous studies [11] that the device is capable to produce SiO_x films using liquid, vaporized siloxanes. When the films are deposited with the recently de-

scribed homogenized plasma mode (locked mode) of the plasma jet [12], a significant improvement of the deposition process with regard to symmetry and homogeneity of the coating and its resulting properties can be achieved. The appearance of self-organized discharge patterns in this mode has been described phenomenologically along with parametric studies on external parameters as applied power, gas flow and electrode distance [13]. Other examples for self-organization phenomena have been described before for both low pressure plasmas and atmospheric pressure dielectric barrier discharges [14–18]. Nevertheless, the explanation of self-organization effects in RF non-thermal atmospheric pressure plasma jets remains hypothetical up to now.

A fundamental plasma physical description of the discharge dynamics requires the knowledge of basic plasma parameters. The current study aims at the determination of the electron concentration and electron temperature in particular in the active discharge zone. These fundamental plasma parameters influence the discharge dynamics and, moreover, the energy transport from the active zone into the effluent where the thin film precursors are produced. The present approach is characterized by a combination of two concepts: the spectroscopic measurement of the broadening of Balmer H_β and H_γ lines and a

^a e-mail: jschaefer@inp-greifswald.de

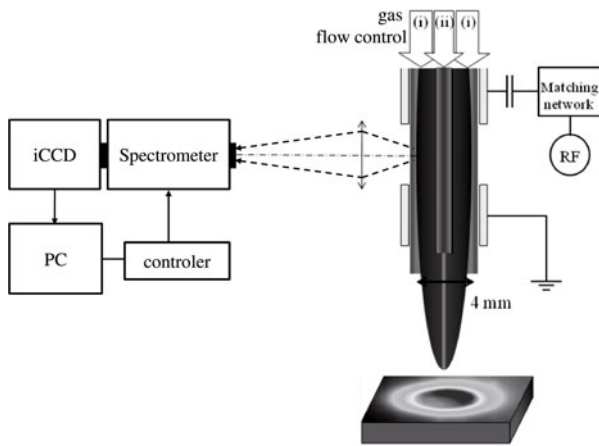


Fig. 1. Schematic drawing of the experimental set-up. The design of the plasma jet illustrates an application situation of stationary film deposition on a flat substrate (right). The spectroscopic arrangement (left) is focused to monitor the active zone in the jet plasma.

time-dependent, spatially two-dimensional fluid model of a single discharge filament. Main features of the experiments and the hydrodynamic model are given.

The explanation of spectral line broadening effects for diagnostic purpose requires profound concern in particular for normal pressure conditions. Hence their influence on the plasma has been evaluated critically considering different broadening models.

2 Experimental set-up

The experiments were carried out using the non-thermal atmospheric pressure jet shown in Figure 1. It has two outer copper ring electrodes around two nested capillaries, which transport gas into the active zone of the jet. Argon (0.3 slm, purity 5.0) is fed to the outer capillary. The inner capillary provides the addition of reactive compounds during thin film deposition experiments, but it was not used in the framework of this paper. The geometric parameters of the source (width and distance of the ring electrodes, and capillary dimensions) are optimized such that a symmetric and spatially homogenized discharge mode (self-organized mode) develops [13]. The inner diameter of the outer capillary is 4 mm and the outer diameter of the inner capillary is 0.8 mm. The experiments reported here were performed with the discharge in locked mode LM3, i.e., three equidistant, stationary filaments rotate regularly with a constant frequency of 80 Hz at the inner wall of the outer capillary. The RF power, measured at the generator (DTG2710, Dressler) was 8 W at 27.12 MHz. Normal laboratory environmental conditions (23 °C, 30% humidity) prevailed during the experiments.

The optical emission of the discharge was measured using a 0.5 m spectrometer (Acton Spectra Pro 2500i, grating 2400 g/mm). An iCCD camera (Pi Max, Princeton Instruments, 1024 × 1024 pixels) at the exit port of the monochromator served as detector. The fine grating along

with a 30 μm entrance slit results in a practical resolving power ($\lambda/\Delta\lambda$) of 1.5×10^4 . The measurements were carried out side on between the two electrodes via glass fiber and collimation lens. The set-up ensures a focus length of 1 cm while maintaining a spatial resolution of 1 mm. The spectra sampling time was kept at 100 ns. Spectra were accumulated over a period of 2×10^3 s.

3 Methods

3.1 Spectral line broadening

Among other effects, collisions of electrons and excited atoms influence the spectral profile of emission lines in a gas discharge. The electron-impact broadening (Stark broadening) is caused by a local perturbation of the electric field. Thus, it can be utilized as a diagnostic method. Several successful experimental and theoretical attempts to evaluate the broadening have been reported in the literature [19–37]. Particularly, the quantification of the electron-impact effect on a suitable combination of spectral lines enables to estimate electron concentration and electron temperature in the plasma [20,26,30,34,37–41].

A proper approach to the electron-impact broadening requires to separate the influence of other broadening mechanisms. Primarily, instrumental broadening, Doppler broadening [23,35], resonance broadening [24], and van der Waals broadening [22,24,36,39] play a relevant role in the practical spectroscopy of atmospheric pressure plasmas. A straightforward concept for the separation of particular broadening components is given e.g. in [39].

The evaluation of the extracted electron-impact broadened line profile originates from the Griem-Kepple model (GK model) [20,25], which bases on the “modified impact theory” [23]. Later, advanced models consider effects of the electron temperature on the line profiles like the model of Czernichowski and Chapelle (CC model) [26,30] and crossing point method reported [38] according to the theory of Griem et al. [20], named GKS model in the following. The CC model bases on the die “unified theory” of line broadening [42,43] generating normalized profiles which cover the whole range from the impact limit in the line centre to the quasi-static limit in the line wings. In the GKS theory [20,25] the Stark broadening is estimated in a quasi-static approximation using the classic Holtsmark field and the ion dynamics is neglected. In the framework of the GKS model reported in [38] two spectral lines spontaneously emitted by the plasma are simultaneously studied in terms of their Stark broadening, which depends on both the electron density and the electron temperature. The comparison between the results for two different lines makes it possible to determine density and temperature of the electrons at the same time. Recently, numerical simulations illuminate the extended, complex influence of other factors like the ion dynamics on the Stark broadening of lines [34,37]. These numerical simulations of Gigoso and Cardenas are referred to as GC model in the following.

In the present study, these four methods, i.e., the GK, CC, GKS and GC model, which reflect the historical

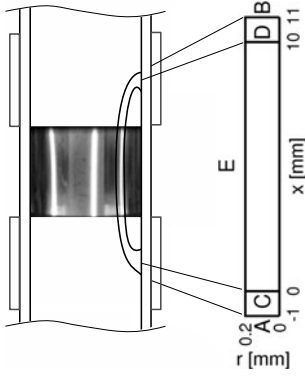


Fig. 2. Simplified geometry as a representation of the filament used for modelling. Boundaries: powered electrode (A), grounded electrode (B), plasma-dielectric interface (C,D) and virtual wall (E).

development of the knowledge of electron-impact broadening, have been applied for the analysis as detailed below in Section 4.2. The electron-impact broadening of Balmer β and γ lines of hydrogen at 486.13 and 434.04 nm, respectively, has been used to determine the electron concentration and electron temperature in the plasma jet of argon. These lines are emitted from hydrogen atoms generated in a dissociation process from residual water vapour. The small amount present in the set-up produces spectroscopically evaluable intensities. Two contributions of the Gaussian profile component (instrumental and Doppler broadening) and a dominant role of electron-impact broadening in the Lorentz profile component of the hydrogen line profiles were assumed. Van der Waals broadening was not considered for numerical reasons. This neglect causes an error in the calculated electron concentration of 10 to 30% [40]. However, the idea of the calculation is focused on the comparison of electron concentrations based on different evaluation models, whose deviations are of the same order as the neglected broadenings effects.

The quantification of the instrumental broadening was obtained experimentally by use of a thulium hollow cathode lamp. The neutral gas temperature, required for the estimation of the Doppler broadening, was estimated spectroscopically from the rotational spectrum of the OH molecule by means of the Boltzmann plot method [44].

3.2 Fluid modelling

The subject of the fluid model is to describe a single filament driven by an RF voltage. Therefore, a simplified two-dimensional geometry, as illustrated in Figure 2, has been used instead of the total set-up shown in Figure 1. The influence of the gas flow on the filament has been neglected in this approach. The simplified geometry is axisymmetric with respect to the axis of the filament. The filament has a length of 10 mm, which corresponds to the distance between the centres of both electrode bands. Dielectrics are attached on both sides of the filament, which represent the wall of the outer quartz capillary. Furthermore, the

Table 1. Reactions considered in the model.

No.	Reaction	Rate coefficient	Ref.
1	$\text{Ar} + e \rightarrow \text{Ar} + e$	$k_1(u_e, n_e)$	BE
2	$\text{Ar} + e \leftrightarrow \text{Ar}^m + e$	$k_2(u_e, n_e)$	BE
3	$\text{Ar} + e \leftrightarrow \text{Ar}^r + e$	$k_3(u_e, n_e)$	BE
4	$\text{Ar} + e \leftrightarrow \text{Ar}^p + e$	$k_4(u_e, n_e)$	BE
5	$\text{Ar} + e \rightarrow \text{Ar}^+ + 2e$	$k_5(u_e, n_e)$	BE
6	$\text{Ar}^m + e \leftrightarrow \text{Ar}^r + e$	$k_6(u_e, n_e)$	BE
7	$\text{Ar}^m + e \leftrightarrow \text{Ar}^p + e$	$k_7(u_e, n_e)$	BE
8	$\text{Ar}^m + e \rightarrow \text{Ar}^+ + 2e$	$k_8(u_e, n_e)$	BE
9	$\text{Ar}^r + e \leftrightarrow \text{Ar}^p + e$	$k_9(u_e, n_e)$	BE
10	$\text{Ar}^r + e \rightarrow \text{Ar}^+ + 2e$	$k_{10}(u_e, n_e)$	BE
11	$\text{Ar}^p + e \rightarrow \text{Ar}^+ + 2e$	$k_{11}(u_e, n_e)$	BE
12	$2 \text{Ar}^m \rightarrow \text{Ar} + e + \text{Ar}^+$	$1.3 \times 10^{-9} \text{ cm}^3 \text{ s}^{-1}$	[45]
13	$\text{Ar}^m + \text{Ar}^r \rightarrow \text{Ar} + e + \text{Ar}^+$	$4.5 \times 10^{-10} \text{ cm}^3 \text{ s}^{-1}$	[45]
14	$2 \text{Ar}^r \rightarrow \text{Ar} + e + \text{Ar}^+$	$4.5 \times 10^{-10} \text{ cm}^3 \text{ s}^{-1}$	[45]
15	$\text{Ar}^r \rightarrow \text{Ar}$	$1.3 \times 10^6 \text{ s}^{-1}$	[46]
16	$\text{Ar}^p \rightarrow \text{Ar}^m$	$1.71 \times 10^7 \text{ s}^{-1}$	[47]
17	$\text{Ar}^p \rightarrow \text{Ar}^r$	$1.64 \times 10^7 \text{ s}^{-1}$	[47]
18	$\text{Ar}^+ + 2 \text{Ar} \rightarrow \text{Ar}_2^+ + \text{Ar}$	$2.5 \times 10^{-31} \text{ cm}^6 \text{ s}^{-1}$	[48]
19	$\text{Ar}_2^+ + e \rightarrow \text{Ar} + \text{Ar}^p$	$1.4 \times 10^{-9} \text{ cm}^3 \text{ s}^{-1}$	[49]
20	$\text{Ar}^m + 2 \text{Ar} \rightarrow \text{Ar}_2^* + \text{Ar}$	$1.3 \times 10^{-32} \text{ cm}^6 \text{ s}^{-1}$	[50]
21	$\text{Ar}^r + 2 \text{Ar} \rightarrow \text{Ar}_2^* + \text{Ar}$	$1.5 \times 10^{-33} \text{ cm}^6 \text{ s}^{-1}$	[50]

BE: determined from solution of 0d Boltzmann equation.

radial extension of the filament is presumed. To limit the filament in radial direction it is assumed to be confined by an outer dielectric surface E at the radius $R = 0.2$ mm. The RF voltage is applied at the outer surface A of the dielectric and the outer surface B is grounded. According to the experimental investigations, a gas temperature of 600 K is used which is assumed to be constant.

The equation system of the hydrodynamic model

$$\frac{\partial}{\partial t} n_l + \nabla \cdot \mathbf{\Gamma}_l = S_l, \quad l = \{e, i, j, m, r, p\} \quad (1)$$

$$\frac{\partial}{\partial t} (n_e u_e) + \nabla \cdot \mathbf{\Gamma}_{eu} = e_0 \mathbf{\Gamma}_e \cdot \nabla V - P^{\text{el}} - P^{\text{in}} \quad (2)$$

$$-\Delta(\epsilon_0 \epsilon_r(x) V) = e_0 (n_i + n_j - n_e) \quad (3)$$

consists of particle balance equations (1) for the densities n_l of the species considered, the electron energy balance equation (2) for the mean electron energy u_e and Poisson's equation (3) for the potential V and electric field $E = -\nabla V$. The model includes electrons ($l = e$), atomic argon ions (Ar^+ , $l = i$) and molecular argon ions (Ar_2^+ , $l = j$) as well as argon atoms excited in metastable (Ar^m , $l = m$), resonance (Ar^r , $l = r$) and higher levels (Ar^p , $l = p$). The particle fluxes of charge carriers having the charge q_l are described in drift-diffusion approximation according to

$$\mathbf{\Gamma}_l = \text{sgn}(q_l) \mu_l n_l \mathbf{E} - D_l \nabla n_l, \quad l = \{e, i, j\} \quad (4)$$

with the mobility μ_l and the diffusion coefficient D_l . Correspondingly, the particle flux of neutral particles $\mathbf{\Gamma}_l = -D_l \nabla n_l$, $l = \{m, r, p\}$ is driven by diffusion only. The source terms S_l in (1) describe gain and loss due to electron impact and heavy particle collisions as well as radiation. These reactions are summarized in Table 1. The rate

coefficients k_l with $l = 1-11$ of the collisions between electrons and argon atoms as well as the electron transport coefficients μ_e and D_e have been prepared as functions of the mean electron energy and the ionization degree by solving the stationary, spatially homogeneous electron Boltzmann equation [51] including electron-electron interaction. The set of electron collision cross sections collected in reference [45] was used to generate the required lumped cross sections of electron collision processes.

Three radiation processes (Nos. 15–17) have been included as indicated in Table 1. For the transition from the resonance state Ar^r to the ground state, the effective lifetime approximation according to the Holstein theory [52] of radiation trapping in an infinite cylinder was applied. The required natural lifetimes have been taken from reference [46].

The energy flux of electrons is described according to $\Gamma_{eu} = (5/3)u_e\mathbf{\Gamma}_e - \chi\nabla u_e$ as a sum of convective flux and thermal diffusion with the coefficient $\chi = (5/3)n_e D_e$. The right-hand-side terms of equation (2) comprise Joule heating and the energy loss rates P^{el} and P^{in} due to elastic and inelastic collisions, which are calculated using the rate coefficients $k_l(u_e, n_e)$. The Poisson equation (3) includes the elementary charge e_0 and the permittivity of free space ϵ_0 . The relative permittivity $\epsilon_r(x)$ is equal to one in the plasma (ϵ_p) and 3.7 in the quartz dielectrics (ϵ_d).

The period-averaged power coupled into the plasma \bar{P}_{tot} is determined according to

$$\bar{P}_{\text{tot}} = \sum_{l=e,i,j} \bar{P}_l, \quad \bar{P}_l = \frac{q_l}{T} \int_0^T \int_V (\mathbf{E} \cdot \mathbf{\Gamma}_l) dV dt \quad (5)$$

by integrating the Joule heating of all charge carriers over the total volume V and by temporal averaging over one period T .

At the transition between the dielectric and the plasma at the boundaries C, D and E (cf. Fig. 2) the change of the electric field from the dielectric to the plasma is related to the surface charge density σ according to

$$\mathbf{n} \cdot (\epsilon_d \mathbf{E}_d - \epsilon_p \mathbf{E}_p) = \sigma \quad (6)$$

where \mathbf{n} denotes the surface normal vector pointing out of the plasma volume and \mathbf{E}_d and \mathbf{E}_p are the electric field vectors in the dielectrics and in the plasma, respectively. The surface charge density is determined by the relation

$$\frac{\partial \sigma}{\partial t} = \sum_{l=e,i,j} q_l \mathbf{\Gamma}_l \cdot \mathbf{n} \quad (7)$$

using the fluxes $\mathbf{\Gamma}_l$ of all charge carriers. Recombination of charge carriers and deexcitation of excited atoms is used as boundary condition at C, D and E. In addition, secondary electron emission $\mathbf{\Gamma}_e = -\gamma(\mathbf{\Gamma}_i + \mathbf{\Gamma}_j)$ with $\gamma = 0.01$ [53] is included at C and D. For the electron energy balance equation the condition $\mathbf{\Gamma}_{eu} = (4/3)u_e\mathbf{\Gamma}_e$ is used at the boundaries C, D and E. At $r = 0$ the axisymmetric symmetry is used as boundary condition. The equation system (1)–(3) is solved using the software CFD-ACE+ [54] with a non-equidistant regular grid and a time step size of $T/4000$.

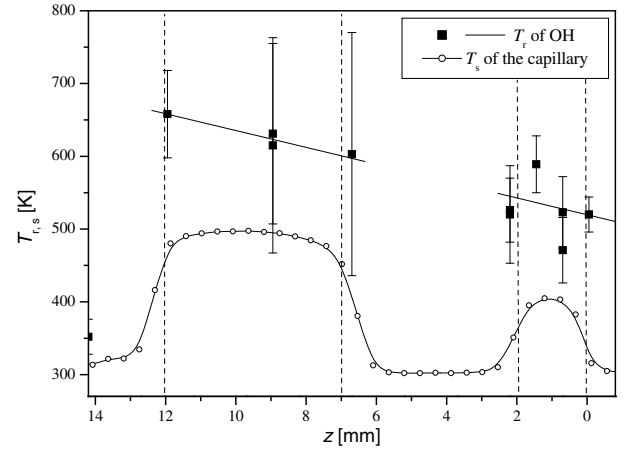


Fig. 3. Approximations of the gas temperature along the jet axis. The dashed z positions mark the end of nozzle (0 mm), grounded electrode (2–7 mm), active plasma zone (7–12 mm), and RF electrode (12–17 mm). The rotational temperature T_r of OH is compared with the surface temperature T_s of the capillary obtained by means of an IR camera under the same conditions [57].

4 Results and discussion

4.1 Doppler broadening and gas temperature

Generally, a spectral profile of lines can be expressed by the well-known Voigt form, which is a convolution of Gaussian and Lorentz dispersion [55]. The quantification of effects determining the Gaussian profile is the first step in order to separate the Lorentz component of the line profile. At atmospheric pressure, the Doppler broadening is the most important pressure-broadening mechanism, which causes the Gaussian character of the line profile. The full width at half maximum (FWHM) of the Doppler broadened line λ_D is given by [23]

$$\Delta\lambda_D = \sqrt{\frac{8 \ln 2 k_B T_g}{m_0 c^2}} \cdot \lambda_0, \quad (8)$$

where k_B is the Boltzmann constant, T_g is the temperature of radiating gas atoms with the mass m_0 , c is the speed of light, and λ_0 denotes the wavelength of the line (in this study H_β or H_γ).

The gas temperature has been approximated by the rotational temperature of OH. Four OH lines of the Q1 branch (307.8444 nm, 307.9951 nm, 308.3278 nm, 308.5196 nm) were selected from collected spectra along the symmetry axis of the jet. The quantum properties of these lines have been taken from [56]. The resulting rotational temperature T_r as a function of the axial position z is shown in Figure 3. The mean value of T_r varies between 500 and 650 K. The real neutral gas temperature T_g remains in the interval (T_s, T_r) limited by the surface temperature T_s of the capillary as a minimum and by the rotational temperature of OH states as a maximum. For the same experimental conditions, the surface temperature T_s of the inner wall has been determined to

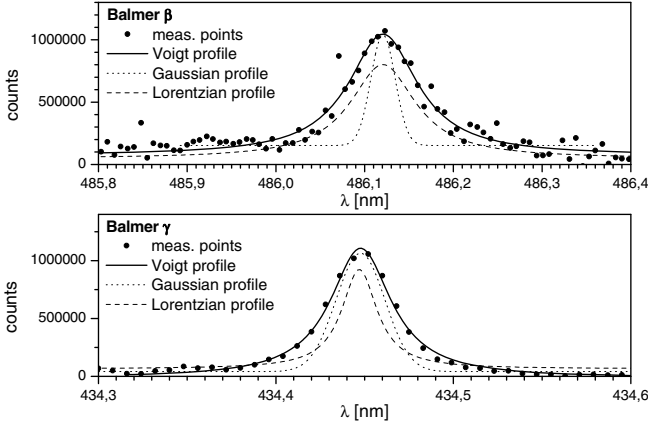


Fig. 4. Broadened profiles of Balmer H_β and H_γ . The intensities of the Gaussian and Lorentzian profiles are not calibrated.

500 K [57]. In the active zone of the plasma jet, the approximation $T_g \approx T_r = 600$ K can be assumed. The measurement enables to quantify the Doppler broadening of H_β and H_γ lines from equation (8) with $\Delta\lambda_D^\beta = 8.5$ pm and $\Delta\lambda_D^\gamma = 7.6$ pm, respectively.

4.2 Electron-impact broadening and plasma parameters

The FWHM of the thermal Doppler broadening $\Delta\lambda_D$ is one of the contributions displaying a Gaussian character of the line profile. The instrumental broadening $\Delta\lambda_a$ is considered, too, as it contributes to the total Gaussian profile. Then, the resulting profile width $\Delta\lambda_G$ can be quantified according to

$$\Delta\lambda_G = \sqrt{\Delta\lambda_D^2 + \Delta\lambda_a^2}. \quad (9)$$

It is possible to deconvolute the Lorentzian part $\Delta\lambda_L$ from the measured Voigt line profile, which is characterized by the FWHM $\Delta\lambda_0$, according to the approximation [38]

$$\Delta\lambda_L \approx \Delta\lambda_0 - \frac{\Delta\lambda_G^2}{\Delta\lambda_0}. \quad (10)$$

The measured lines and corresponding profiles are plotted in Figure 4. The results of the deconvolution are listed in Table 2. The Lorentz component $\Delta\lambda_L$, which is equal to the electron-impact broadening $\Delta\lambda_S$ of the hydrogen emission lines in the present approximation, has been calculated according to (10) using (9).

As mentioned above, four different methods were applied for the evaluation of the electron-impact broadening in order to obtain the electron concentration and electron temperature of the plasma jet. The selection of the applied methods reflects the historical development of the knowledge on the electron-impact broadening. Griem's theory and tables of hydrogen line broadening involved in the

Table 2. Broadening components of measured hydrogen lines. The spectrum has been measured at the position $z = 9$ mm in the center of the active zone (cf. Fig. 3).

Emission line	H_β ($2p-4d$)	H_γ ($2p-5d$)
Wavelength λ_0	486.13 nm	434.04 nm
FWHM $\Delta\lambda_0$	103 pm	43 pm
Instrumental broadening $\Delta\lambda_a$	32 pm	29 pm
Doppler broadening $\Delta\lambda_D$	9 pm	8 pm
Gaussian FWHM $\Delta\lambda_G$	33 pm	30 pm
Lorentz FWHM $\Delta\lambda_L$	92 pm	22 pm

GK and GKS model represent the fundamentals for the spectroscopic application of the electron-impact broadening. In the simplified version of the data evaluation, i.e., the GK model [20,25], only the Balmer β line has been evaluated, since the electron-impact broadening of H_β is less sensitive to the electron temperature and can be used for its direct estimation. This concept has been extended by the corresponding electron temperature correction in the CC model [26,30].

The advanced application of Griem's theory results in the crossing point method (GKS model) [38], which considers the electron-impact broadening of two lines, here Balmer β and Balmer γ , and determines both the electron concentration and temperature. The data processing method has been updated in [38] according to [27]. However, the unit system remains heterogeneous, which makes the calculation method unclear. Therefore, the central relations of the GKS model are given here for both spectral lines. The estimation of the electron-impact line broadening in a quasi-static approximation using the classic Holtzmark field according to [20,25] results in the relation

$$n_e = \frac{15}{4} \left(\frac{\Delta\lambda_S^q \cdot 10^9}{2\pi\alpha_{1/2}^q(n_e, T_e)} \right)^{3/2}, \quad q = \{\beta, \gamma\}, \quad (11)$$

where n_e is the electron concentration in cm^{-3} and $\Delta\lambda_S^q$ is the electron-impact broadened FWHM of Balmer line in \AA where q denotes the Balmer β and γ line, respectively. The parameter $\alpha_{1/2}^q(n_e, T_e)$, depending on the electron density and temperature, is the reduced wavelength difference in the unit $\text{\AA} \text{Fr} \text{s}^2 \text{g}^{-1} \text{cm}^{-2}$. It is listed in Griem's tables for Balmer lines in the same unit in [27]. The graphical solution of equation (11) for the Balmer β and γ line with the crossing-point method is shown in the left part of Figure 5. The GKS model leads to an electron concentration of 2.4 to $3.0 \times 10^{14} \text{ cm}^{-3}$ and an electron temperature between 20000 and 30000 K in the active zone of the plasma jet. The crossing point has been estimated with an accuracy of 30% regarding the neglected van der Waals broadening.

In an attempt to involve the influence of the ion dynamics, newer tables of hydrogen line broadening based on numerical simulations (GC model) have been published and compared with experimental results [34]. The relative deviation between the GC model and the CC model was found to be about 20% [40]. The variation of the electron concentration on the electron-impact broadening of the Balmer β line using the GC model is shown in the right

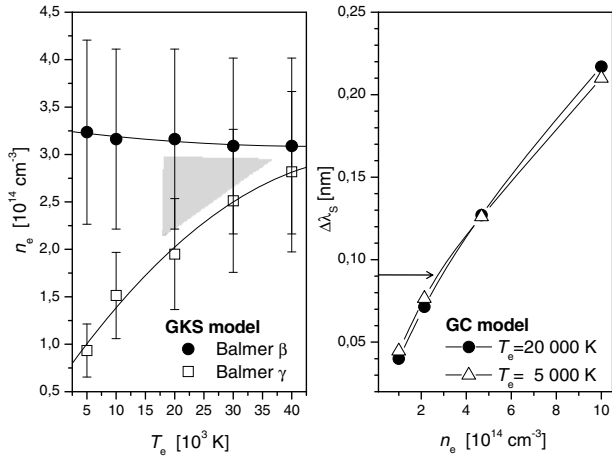


Fig. 5. Estimation of electron concentration and temperature. Application of GKS model and crossing point method on the measured spectra (left). Estimation of electron concentration using the GC model applied on the measured Balmer β line (right).

Table 3. Electron concentration based on electron-impact broadening of hydrogen lines of Balmer series and comparison with fluid modelling results. The references are linked to the respective model applied in the determination.

Method	n_e (cm^{-3})	Reference
GKS model	2.7×10^{14}	[27,38]
GK model	3.3×10^{14}	[20,25]
CC model	2.2×10^{14}	[26,30]
GC model	3.0×10^{14}	[34,37]
Fluid model	7.2×10^{13}	Section 4.3

part of Figure 5 for two electron temperatures. The electron concentration resulting for the $\Delta\lambda_S^\beta = 92$ pm is about $3.0 \times 10^{14} \text{ cm}^{-3}$.

The results of the electron concentration obtained by applying the four different models and by fluid model calculations using the method described in Section 3.2 are presented in Table 3. The values for the electron concentration obtained from the GKS, GK, CC and GC model are all in the interval from 2.2 to $3.3 \times 10^{14} \text{ cm}^{-3}$. All values are in the validity interval of these models and their presumptions are fulfilled in the experiment and calculation. Particularly, the impact approximation [19], on which all models on the electron-impact broadening are based, is positively approved for the presented results.

4.3 Results of the fluid model

Results of the model calculations of the filament are shown in Figures 6–8. The RF voltage has been adjusted to obtain a total period-averaged power \bar{P}_{tot} of 1.3 W. This value corresponds to one third of the power dissipated in the plasma which is assumed to be half of the supplied

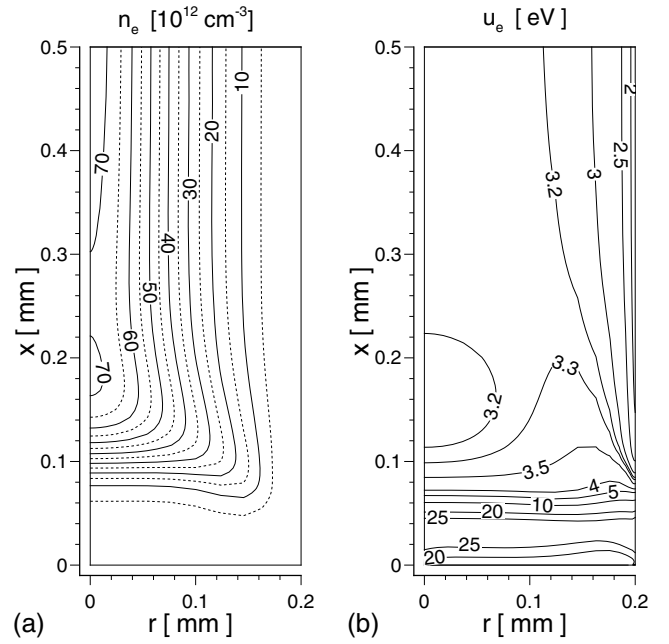


Fig. 6. Period-averaged electron density (a) and mean electron energy (b).

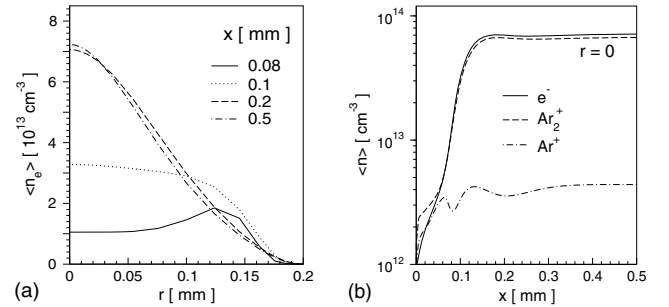


Fig. 7. Period-averaged densities of charge carriers: radial profiles of the electron density at different axial positions x (a) and axial profiles of the densities of electrons and ions (b).

power of 8 W. The figures show only the axially inhomogeneous transition region from the dielectric surface at $x = 0$ to $x = 0.5$ mm. Apart from this region, the filament is nearly axially homogeneous.

4.3.1 Charge carriers

Figures 6a and 7a illustrate the structural change of the period-averaged electron density from the sheath near the dielectric to the column. The strong electric field in the sheath leads to a more flat density profile, whereas a pronounced profile is caused in the column due to ambipolar diffusion. The period-averaged electron density reaches a value of about $7.2 \times 10^{13} \text{ cm}^{-3}$ in the centre. This value is about 30% of the result deduced from the measurements (cf. Tab. 3).

The period-averaged mean electron energy is shown in Figure 6b. In the column the mean electron energy

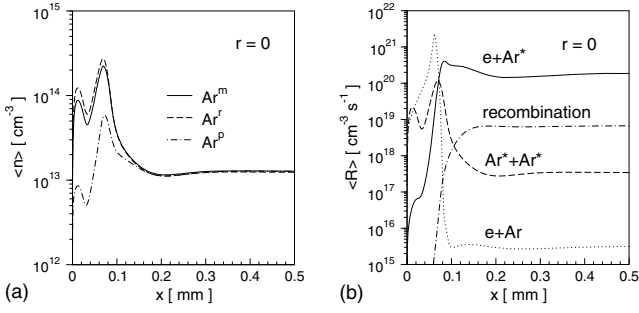


Fig. 8. Period-averaged axial profiles of excited atom densities (a) and of ionization rates at $r = 0$ (b): ionization in electron collisions with ground state atoms (R5, dotted line) and with excited atoms (R8 + R10 + R11, full line), chemo-ionization (R12 + R13 + R14, dashed line) and recombination (R19, dashed-dotted line). R: reaction No.

has a radial profile which is more flat than the density profile shown in Figure 7a. Its maximal value is about 3.2 eV on average and oscillates with an amplitude of about 20%. The period-averaged value corresponds to an electron temperature $T_e = (2/3)u_e/k_B$ of about 22 400 K which is in reasonable agreement with the result from the experiment (cf. Fig. 5) taking into account the uncertainties of both approaches. In the sheath the mean electron energy strongly increases to large values of about 28 eV due to the large electric field and the resultant enhanced energy gain of the electrons.

The period-averaged axial density profiles of charge carriers are depicted in Figure 7b. The molecular ions Ar_2^+ represent the dominant positive charge carrier in nearly the total volume. This is caused by the large rate coefficient of the reaction $\text{Ar}^+ + 2\text{Ar} \rightarrow \text{Ar}_2^+ + \text{Ar}$. Only in the sheath very near to the dielectric surface ($x < 0.04$ mm), where the ionization due to electron collisions with ground state atoms is very pronounced, the density of atomic ions Ar^+ exceeds slightly that of the electrons.

4.3.2 Excited species

The period-averaged axial density profiles of excited atoms at $r = 0$ are displayed in Figure 8a. The profile of the excited atoms have a large peak in the sheath which reflects the increase of the mean electron energy in this region as shown in Figure 6b. Similar profiles have been obtained for the metastable and resonance atoms Ar^m and Ar^r with maximal densities of about $2 \times 10^{14} \text{ cm}^{-3}$ in the sheath and about 10^{13} cm^{-3} in the column.

The axial profiles of the ionization rates are shown in Figure 8b. The full line marks the most important ionization channel which is the ionization rate due to electron collisions with excited atoms. Compared to this ionization channel, the chemo-ionization due to collisions between excited argon atoms Ar^m , Ar^r and Ar^p is lower by more than two orders of magnitude in the column. However, its contribution is important in the sheath where the excited atom densities have their peak. Furthermore, the ioniza-

tion due to electron collisions with ground state atoms is dominant in the sheath due to the large mean electron energy and large reaction rate coefficients, but it becomes unimportant in the column.

5 Summary

The self-organization mode is a distinctive discharge regime of the RF non-thermal atmospheric pressure plasma jet which produces a foot print of the discharge symmetric with respect to the axis of the jet that ultimately leads to an enhanced homogeneity of the deposited films. The study is focused on the determination of basic parameters of the plasma in the active zone of the jet between the RF electrodes. The electron concentration and temperature were determined in this region by experiments and model calculations.

The spectroscopic measurement uses the emission from hydrogen atoms originating from residual water vapour in the gas phase. The theory of spectral line broadening has been applied to obtain the plasma parameters. For this purpose, four different models have been used, namely the so-called CC, GC, GK and GKS model. The values of the electron concentration obtained by these models are distributed in the interval from 2.2 to $3.3 \times 10^{14} \text{ cm}^{-3}$. The influence of those broadening effects which have not been considered is negligible compared to the width of this interval. The electron temperature can only be roughly determined by the applied method. The value of 20 000 to 30 000 K resulting from the GKS model is an approximation at the highest confidence probability. However, it is difficult to specify the magnitude of this probability.

The experiments have been complemented and evaluated by model calculations using a time-dependent, spatially two-dimensional fluid model of a single filament in the jet drive by an RF voltage. A broad radial profile with a maximal value in the centre of about 22 000 K has been found in the column of the filament. Moreover, an electron concentration of about $7 \times 10^{13} \text{ cm}^{-3}$ in the centre of the filament has been obtained by the fluid model, which is roughly the same order of magnitude as the spectroscopic results. The modulation of the density and mean energy of the electrons has been found to be very small in the column. This finding of the model calculations supports the time-averaged determination of these quantities by the spectroscopic method.

In addition, the fluid model calculations have revealed the structural change of the filament from the dielectric surface through the sheath to the column. This axially inhomogeneous region has an extension of about 0.5 mm at the discharge conditions considered. For the excited atoms a concentration of about 10^{13} cm^{-3} has been found in the column, where the ionizing collisions of electrons with excited atoms represent the most important ionization channel.

The relatively high electron concentration in the active zone of the jet can be explained by the contraction of the discharge in single filaments. Due to the self-organization, these filaments are not stochastic but deterministic with a

long lifetime which supports the establishment of a larger concentration of excited atoms, especially metastable atoms, leading to enlarged ionization.

The deviation of the fluid model result for the electron concentration from the measured ones may be caused by the limitation of both approaches. Improvements are expected from further investigations which overcome these limitations by including e.g. the van der Waals broadening in the spectroscopic method and the influence of the gas heating and contraction mechanism in the fluid model.

The work was supported in part by the Deutsche Forschungsgemeinschaft within SFB-TR 24. We thank Sebastian Peters for his help at data collection.

References

1. A. Schütze, J.Y. Yeong, S.E. Babayan, J. Park, G.S. Selwyn, R.F. Hicks, *IEEE Trans. Plasma Sci.* **26**, 1685 (1998)
2. S.E. Babayan, J.Y. Jeong, V.J. Tu, J. Park, G.S. Selwyn, R.F. Hicks, *Plasma Source. Sci. Technol.* **7**, 28 (1998)
3. J. Janča, M. Klima, P. Slaviček, L. Zajičková, *Surf. Coat. Technol.* **116**, 547 (1999)
4. J. Kousal, Z. Pokorna, A. Brablec, P. Slaviček, M. Klima, J. Janča, *Czech. J. Phys.* **52**, 571 (2002)
5. P. Slaviček, A. Brablec, V. Kapička, M. Klima, M. Šira, *Acta Phys. Slovaca* **55**, 573 (2005)
6. R. Foest, E. Kindel, A. Ohl, M. Stieber, K.-D. Weltmann, *Plasma Phys. Control. Fusion* **47**, B525 (2005)
7. R. Foest, E. Kindel, H. Lange, A. Ohl, M. Stieber, K.-D. Weltmann, *Contrib. Plasma Phys.* **46**, 119 (2007)
8. J. Benedikt, V. Raballand, A. Yanguas-Gil, K. Focke, A. von Keudell, *Plasma Phys. Control. Fusion* **49**, B419 (2007)
9. M. Laroussi, T. Akan, *Plasma Processes. Polym.* **4**, 777 (2007)
10. K.H. Becker, U. Kogelschatz, K.H. Schoenbach, R.J. Barker, *Non-equilibrium air plasmas at atmospheric pressure* (Institute of Physics Publishing, Bristol, 2005)
11. J. Schäfer, R. Foest, A. Quade, A. Ohl, K.-D. Weltmann, *Eur. Phys. J. D* **54**, 211 (2009)
12. J. Schäfer, R. Foest, A. Quade, A. Ohl, K.-D. Weltmann, *J. Phys. D* **41**, 194010 (2008)
13. J. Schäfer, R. Foest, A. Ohl, K.-D. Weltmann, *Plasma Phys. Control. Fusion* **51**, 124045 (2009)
14. Y.A. Gostinstev, *Fluid Dyn.* **4**, 158 (1969)
15. K.G. Müller, *Phys. Rev. A* **37**, 4836 (1988)
16. I. Müller, E. Ammelt, H.-G. Purwins, *Phys. Rev. Lett.* **82**, 3428 (1999)
17. K.H. Schoenbach, M. Moselhy, W. Shi, *Plasma Source. Sci. Technol.* **13**, 177 (2004)
18. A. Brockhaus, R. Sauerbier, J. Engemann, *Eur. Phys. J. Appl. Phys.* **47**, 22809 (2009)
19. H.A. Lorenz, *Proc. R. Acad. Sci.* **8**, 591 (1906)
20. H.R. Griem, A.C. Kolb, K.Y. Shen, *Astrophys. J.* **135**, 272 (1962)
21. H.R. Griem, M. Baranger, A.C. Kolb, G. Oertel, *Phys. Rev.* **125**, 177 (1962)
22. C.W. Allen, *Astrophysical Quantities* (The Athlone Press, London, 1964)
23. H.R. Griem, *Plasma Spectroscopy* (Mc Graw-Hill, New York, 1964)
24. A.W. Ali, H.R. Griem, *Phys. Rev. A* **140**, 1044 (1965)
25. P. Kepple, H.R. Griem, *Phys. Rev.* **173**, 317 (1968)
26. C.R. Vidal, J. Cooper, E.W. Smith, *Astrophys. J.* **25**, 37 (1973)
27. H.R. Griem, *Spectral Line Broadening by Plasmas* (Academic Press, 1974)
28. N. Konjevic, J.R. Roberts, *J. Phys. Chem. Ref. Data* **5**, 209 (1976)
29. N. Konjevic, W.L. Wiese, *J. Phys. Chem. Ref. Data* **5**, 259 (1976)
30. A. Czernichowski, J. Chapelle, *Acta Phys. Pol. A* **63**, 67 (1983)
31. N. Konjevic, M.S. Dimitrijevic, W.L. Wiese, *J. Phys. Chem. Ref. Data* **13**, 619 (1984)
32. N. Konjevic, W.L. Wiese, *J. Phys. Chem. Ref. Data* **19**, 1307 (1990)
33. R.F.G. Meulenbroeks, M.F.M. Steenbakkens, Z. Qing, M.C.M. van de Sanden, D.C. Schram, *Phys. Rev. E* **49**, 2272 (1994)
34. M.A. Gigosos, V. Cardenosos, *J. Phys. B: At. Mol. Opt. Phys.* **29**, 4795 (1996)
35. R. Konjevic, N. Konjevic, *Spectrochim. Acta B* **52**, 2077 (1997)
36. C. Trassy, A. Tazzen, *Spectrochim. Acta B* **54**, 581 (1999)
37. M.A. Gigosos, M.A. Gonzales, V. Cardenoso, *Spectrochim. Acta B* **58**, 1489 (2003)
38. J. Torres, J. Jonkers, M.J. van de Sade, J.J.A.M. van der Mullen, A. Gamero, A. Sola, *J. Phys. D* **36**, L55 (2003)
39. C. Yubero, M.D. Calzada, M.C. Garcia, *J. Phys. Soc. Jpn* **74**, 2249 (2005)
40. C. Yubero, M.C. Garcia, M.D. Calzada, *Spectrochim. Acta B* **61**, 540 (2006)
41. J. Torres, J.M. Palomares, A. Sola, J.J.A.M. van der Mullen, A. Gamero, *J. Phys. D* **40**, 5929 (2007)
42. E.W. Smith, J. Copper, C.R. Vidal, *Phys. Rev.* **185**, 140 (1969)
43. D. Voslamber, *Z. Naturforsch.* **24a**, 1458 (1969)
44. C. de Izara, *J. Phys. D* **33**, 1697 (2000)
45. S. Gorchakov, D. Loffhagen, D. Uhrlandt, *Phys. Rev. E* **74**, 066401 (2006)
46. G.M. Lawrence, *Phys. Rev.* **175**, 40 (1968)
47. W.L. Wiese, J.W. Brault, K. Danzmann, V. Helbig, M. Kock, *Phys. Rev. A* **39**, 2461 (1989)
48. T. Johnson, A. Hunter, *J. Appl. Phys.* **51**, 2406 (1980)
49. J. Royal, A.E. Orel, *Phys. Rev. A* **73**, 042706 (2006)
50. P. Millet, A. Birot, H. Brunet, H. Dijolis, J. Galy, Y. Salamero, *J. Phys. B: At. Mol. Phys.* **15**, 2935 (1982)
51. H. Leyh, D. Loffhagen, R. Winkler, *Comput. Phys. Commun.* **113**, 33 (1998)
52. T. Holstein, *Phys. Rev.* **72**, 1212 (1947)
53. N. Balcon, G.J.M. Hagelaar, J.P. Boeuf, *IEEE Trans. Plasma Sci.* **36**, 2782 (2008)
54. <http://www.esi-cfd.com>, accessed in May 2010
55. K. Hunger, *Z. Astrophys.* **39**, 36 (1956)
56. G.H. Diecke, H.M. Crosswhite, *J. Quant. Spectrosc. Radiat. Transfer* **2**, 97 (1961)
57. J. Schäfer, A. Vogelsang, R. Foest, A. Ohl, *Proc. 19th ISPC* (Bochum, 2009), ID 298